Pitting corrosion study at the built and substrate region of hybrid additive-manufactured Al-Si-Mg alloys

Samson Dare Oguntuyi[1*], *Mandlenkosi G.R.* Mahlobo[2], *Kasongo* Nyembwe[3], *Peter M.* Mashinini[4] and *Peter* Olubambi[1]

[1]Centre for Nanoengineering and Advanced Materials (CeNAM), School of Mining, Metallurgy and Chemical Engineering, University of Johannesburg, Johannesburg, 2092, South Africa
[2]Department of Chemical and Materials Engineering, University of South Africa, P.O. Box 392, Florida 1709, South Africa
[3]Department of Mechanical and Mechatronic Engineering, Cape Peninsula University of Technology, Cape Town, South Africa.
[4]Department of Mechanical and Industrial Engineering, University of Johannesburg, Doornfontein Campus, Johannesburg 2028, South Africa

Abstract. Hybrid Additive Manufacturing (HAM) of Al-Si-Mg alloys results in distinct microstructural variations at the built-substrate interface, influencing electrochemical behavior and overall performance. This study investigates the characteristics and corrosion response of as-received built-substrate HAM Al-Si-Mg alloys through microstructural and electrochemical analysis. Thorough microstructural evaluation was carried out using scanning electron microscopy (SEM), and energy-dispersive X-ray spectroscopy (EDS), to determine grain morphology and phase distribution in the built and substrate zones. Open circuit potential (OCP), cyclic potentiodynamic polarization (CPP) and electrochemical impedance spectroscopy (EIS) were employed to assess corrosion resistance and pitting susceptibility in natural seawater. The findings provide insights into the role of interfacial microstructure on corrosion susceptibility, contributing to the optimization of HAM-processed Al-Si-Mg alloys for enhanced performance in engineering applications. The outcome revealed that the substrate area showed a refined microstructure with enhanced corrosion resistance in contrast to the built. Also, this study gives a vital understanding of the corrosion behaviour of each region of HAM Al-Si-Mg alloys, which is important for service reliability and structural integrity in aerospace and marine applications.

1 Introduction

The fabrication of metallic parts has been revolutionized by additive manufacturing (AM), due to its ability to minimize material waste, enable the production of complex geometries, and offer tailored design flexibility [1]. Among the various AM methods, Laser Powder Bed

* Corresponding author: samsoniumdare@gmail.com

Fusion (LPBF) and Direct Energy Deposition (DED) have gained significant recognition for manufacturing lightweight aluminum alloy parts, particularly in Al-Si-Mg structures. This is attributed to their excellent castability, high strength-to-weight ratio, and good corrosion resistance. These alloys are commonly used in the aerospace, automotive, and marine industries, where environmental toughness and mechanical integrity are critically important [2]. However, the full integration of AM parts remains limited by challenges such as residual stresses, anisotropic properties, and microstructural inhomogeneities in the materials printed. To overcome these limitations, Hybrid Additive Manufacturing (HAM) has emerged as a promising approach, whereby additive techniques can be combined with subtractive or traditional fabrication processes [3, 4].

In HAM, AM is applied to produce a component on a cast or wrought substrate, hence integrating the importance of both methods. Though it provides enhanced performance and functional products, it brings new complications. This includes, in particular, microstructural changes, metallurgical incompatibilities, and corrosion initiation at the built-substrate interface [5, 6]. The microstructure of these alloys is hugely affected by the thermal cycling, quick solidification rates, and complex heat-affected zones developed during the layer-by-layer deposition. These issues produce silicon particle separation which result in refined grain structures and secondary phase redistribution. Consequently, this influences the corrosion behaviour, categorically pitting corrosion. Pitting is a harsh and localized type of attack in chloride-rich surroundings [7, 8]. This can promote microstructural defects like porosity, intermetallic particles or altered grain boundaries. Also, there is a likelihood of thermal variation-induced stresses, microstructural variation, and localized galvanic couples that could aggravate pitting vulnerability [4].

Many works have evaluated the microstructure, corrosion, and mechanical performance of AM Al-Si-Mg alloys [9-11] also even the successful utilization of HAM for different components has been achieved, with various researchers evaluating their microstructure, and mechanical properties [12-14]. However, to date, no studies have been found to be carried out on the corrosion performance at the built and substrate regions in HAM components. The relationship between microstructural characteristics and electrochemical response in this changing region is considered of high important for envisaging service life and assuring the structural integrity of HAM parts being opened to corrosive surroundings.

Therefore, this study aims to occupy this knowledge gap by carrying out a microstructural and electrochemical examination of both the built and substrate regions of hybrid additive manufactured components. The findings provide valuable insights into the corrosion mechanisms and identify key factors influencing corrosion resistance in HAM Al-Si-Mg alloys.

2 Methodology

2.1 Sample fabrication and preparation

To create the dissimilar aluminium alloy combinations for this study, a selective laser melting (SLM) metal 3D printer (Model FS121M) manufactured by Farsoon Technologies, Changsha, China, was used. The process involved building rectangular-shaped layers of Al 7 and Al 10 alloys parts 10 x 10 x 10 mm directly on cast substrates, which were water-quenched castings of Al 6061 alloys. These were placed on a larger rectangular base measuring 50 × 50 × 50 mm. The chemical compositions of the Al 7 and Al 10 powders used in the build, each with an average particle size ranging from 20 to 50 μm were provided in Table 1. Figure 1 depicts how the samples for each analyses were sectioned.

Table 1. The compositions of the Hybrid components (Built and substrates)

Alloys	Elements							
	Fe	Mn	Cu	Zn	Si	Cr	Mg	Al
Al 7	0.10	0.15	0.25	0.50	7.00	0.10	0.40	Remaining
Al 10	0.10	0.15	0.25	0.50	10.00	0.40	0.10	Remaining
Al 6061	0.35	0.15	0.25	0.10	0.70	0.20	1.00	Remaining

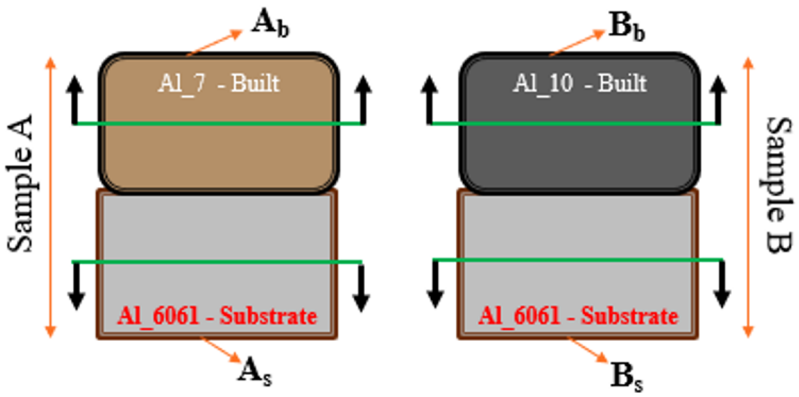

Fig. 1. Schematic diagram of the hybrid sample, indicating how it was sectioned.

The SLM build process was carried out using the following parameters: a laser power of 370 W, a substrate temperature of 200 °C, a scanning speed of 1300 mm/s, a hatch spacing of 190 µm, and a powder layer thickness of 30 µm. A stripe hatch strategy was employed with a 67° rotation between successive layers to ensure optimal microstructural uniformity and bonding.

Before SEM and electrochemical evaluation, the sample cross-sections were metallographically prepared and cold-mounted using epoxy resin. They were then ground with silicon carbide (SiC) papers of varying grits and subsequently polished to a surface finish of 1 µm using a diamond suspension.

2.2 Electrolyte solution

In simulating a practical marine corrosive environment, a natural seawater was applied as the electrolyte, instead of the commonly used laboratory-prepared 3.5 wt.% NaCl solution. The seawater was collected from Porth Elizabeth, South Africa, and applied without any modification. Its natural ionic and chloride content (of approximately 1.9 wt.% Cl^-) gives a typical harsh medium for examining the electrochemical performance and corrosion resistance of aluminium alloys in the typical South African marine environment by the Indian Ocean. This scientific route makes the study more applicable to real-world marine environments as well as other areas where materials may be susceptible to similar corrosion.

2.3 Electrochemical tests

Electrochemical evaluations were conducted via a standard three-electrode arrangement, comprising a saturated calomel electrode (SCE) as the reference, a platinum electrode as the counter electrode, with the examined samples serving as the working electrode. All the potentials stated in this work are referenced to the SCE scale. Polarization curves were achieved via EG&G 273A potentiostat, operated by the SoftCorr M352 software, with the electrode potential automatically ranging at a scan rate of 0.166 mV/s. All experiments were done at Standard Temperature and Pressure (STP).

Before starting the polarization scan, the Al alloy samples were first inserted in the solution to ensure the OCP was normalized. It was discovered that after 2 hr of insertion, the OCP readings remained consistent within a range of ±20 mV, in contrast to readings taken over several hours. Based on this, a 2-hr insertion duration was identified as the standard stabilization time for all subsequent electrochemical examinations.

After the 2-hr duration of the insertion, electrochemical measurements were developed to examine the corrosion performance of the alloy in the natural seawater. EIS was performed at the OCP. The examination was carried out via the application of a sinusoidal AC signal with an amplitude of 10 mV (peak-to-peak), and impedance response was calculated over a frequency variation from 0.1 Hz to 10^5 Hz. This ensured that the direct attainment of phase shift (θ) values and impedance (Z) in the frequency area, making it for electrochemical kinetics and charge transfer resistance to be easily analysed under potentiostatic and open circuit situations.

Afterward, cyclic potentiodynamic polarization (CPP) tests were developed to examine the built and substrate vulnerability to localized corrosion directly relating to pitting susceptibility. The scan commences at 250 mV below the stabilized OCP and progresses anodically at a scan rate of 0.5 mV/s up to a vertex potential of +1.0 V vs. Ag/AgCl. After reaching this potential, the scan direction was reversed in the cathodic direction until the scan returned to the initial potential. To avoid excessive dissociation, a vertex current density of 0.001 A/cm² was used. The cyclic scan ensured the critical potentials identification, like pitting potential (E_{pit}) and the repassivation potential (E_{rep}), essential for evaluating the pitting performance of the alloy.

2.4 Microstructural analysis

A JSM-7900F scanning electron microscope (SEM) equipped with EDS was used to examine the microstructure and composition of the samples before corrosion. Secondary electron (SE) images taken during the SEM analyses were also employed to assess pitting corrosion features and to characterize the corrosion products formed after exposure to the seawater.

3 Results and discussion

3.1 Electrochemical tests

3.1.1 Open circuit potential

Figure 2 depicts the graph of the OCP variation over time of two hybrid samples, namely: Sample A and Sample B. In each of these samples, the two areas examined were the built and a substrate. The substrate and the built area, denoted for each sample are A_b, A_s, B_b, and B_s.

Ideally, the more negative values an OCP has for a sample the higher the rate of corrosion [15, 16]. Hence Figure 2, reveals that built samples exhibited a high corrosion resistance in contrast to the substrates. However, in relation to pitting corrosion, the range of values of the examined samples has some contrasting outcomes. Although samples A_b and B_b exhibited less negative values compared to samples A_s and B_s, the range of their values was a better indication of their susceptibility to different corrosion mechanisms [17]. Considering the range of OCP values for each sample, the substrate samples revealed more stable and consistent behavior in withstanding pitting corrosion. For sample A, the substrate region (A_s) shows a relatively stable potential range between approximately –0.775 V and –0.755 V. This narrow range and limited noise suggest fair susceptibility and electrochemical stability to corrosion in the substrate region of sample A. The built region of sample A, denoted as A_b, exhibited a wider and more unstable potential which ranged from approximately value of –0.735 V to –0.700 V, with irregular peaks reaching up to –0.685 V. The negative potential values and increased noise reveal that the built area of sample A is more electrochemically active (indicating active surface behaviour and thus poor passivation) and potentially more prone to pitting corrosion than the substrate. For sample B, the substrate region (B_s) displays the most stable negative potential values, ranging about –0.780 V to –0.765 V. This performance suggests excellent corrosion resistance to pitting corrosion and electrochemical stability in the substrate portion of sample B. According to Tan et al. (2009) [18], a plot depicting huge differences in OCP, such as those observed for samples A_b and B_b, typically indicates a greater level of pitting activity on the material surface.

The built region of sample B, denoted as B_b, reveals a potential range between –0.755 V and –0.735 V. While the potential was less stable than that of the substrate region, it was also more stable and less noisy in contrast to the built region of Sample A, which indicated moderately to good electrochemical performance. Andreatta et al (2004) [19] stated that low noise in the OCP signal suggests that localized corrosion attacks, such as pitting or micro-cracking, are minimal or even absent. Therefore, despite the fact that the substrate regions of both Sample A and Sample B exhibited more OCP negative values than their respective built regions, their stable OCP values implied better corrosion resistance to pitting in the aggressive environments exposed to in this study [19]. Among all, the substrate region of Sample B (B_s) demonstrates the most stable negative potential, which signified the optimal corrosion resistance. In contrast the built region of Sample A (A_b) revealed the maximum electrochemical noise and the least corrosion resistance based on its OCP performance. Also, the built samples A and B were more susceptible to localized corrosion occurrence (pitting) due to a less uniform (or defective) passive film formation, which was in contrast to their substrate counterparts [18, 19].

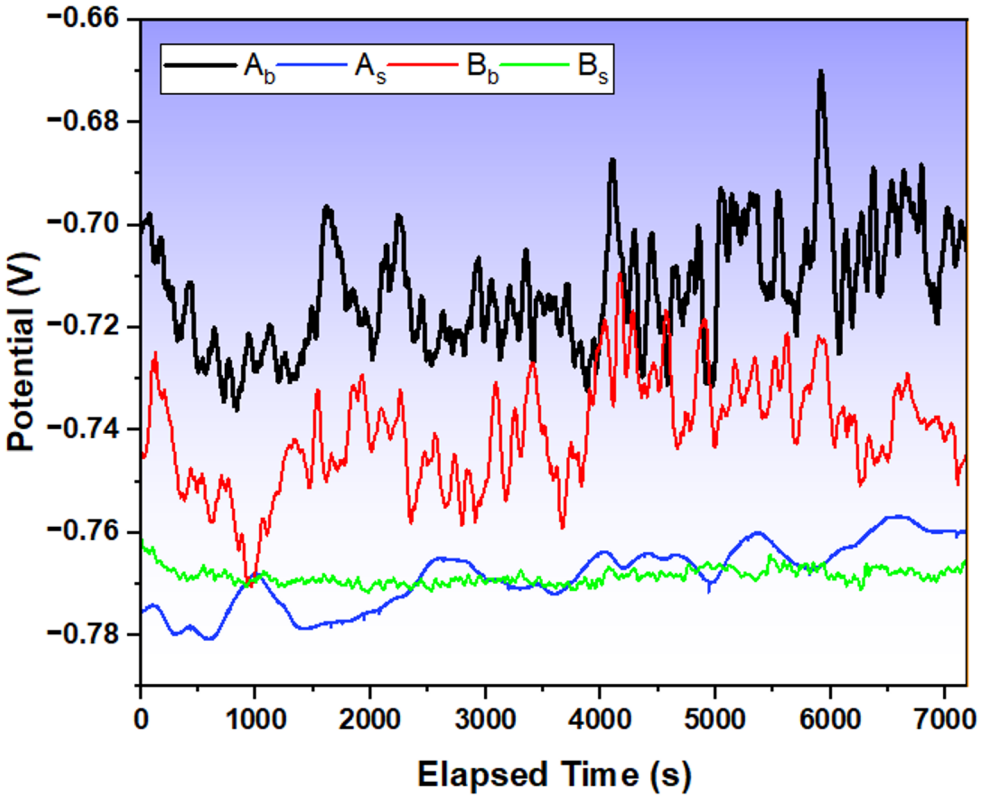

Fig. 2. Circuit polarization curves for the built and substrate samples immersed in a typical seawater.

3.1.2 Electrochemical impedance spectroscopy (EIS) analysis

Figure 3 showed the Bode graph from EIS evaluations. The different impedance performances among the examined samples, were compared. At high frequencies, all samples join to the same low impedance values, suggesting comparable solution resistance (Rs) across the diverse systems. This indicates that the electrolyte conductivity and composition were steady during measurements [20, 21].

Significant variations occurred at low frequencies, where the impedance was controlled by charge transfer resistance (Rct), which depicted the corrosion stability and electrochemical stability of every sample [21]. The substrate of sample A (A_s) demonstrated the optimum impedance response, which revealed the best corrosion resistance among the examined samples. This was followed by the built area of sample B (B_b), and the substrate of sample B (B_s), both of which revealed modest impedance values, signifying a comparatively steady while less shielding passive layer in contrast to A_s. However, the consistency and stability of their electrochemical responses highlighted the difference in their individual corrosion behaviours, since B_s had less noise than B_b, which was indicative of improved resistance to localized corrosion.

In comparison, the built section of sample A (A_b) depicted the lowest impedance and imbalance performance at low frequencies, with variations and a significant decline in impedance that was characteristic of corrosion mechanisms such as localized pitting or disintegration of the passive layer being present. The irregular impedance performance of A_b also suggests a lesser corrosion shield and poor electrochemical stability relative to the other samples [22]. These findings show that the substrate materials of the alloy exhibit higher

corrosion resistance in contrast to their built counterparts, with A_s giving the superior effective shield to charge transfer.

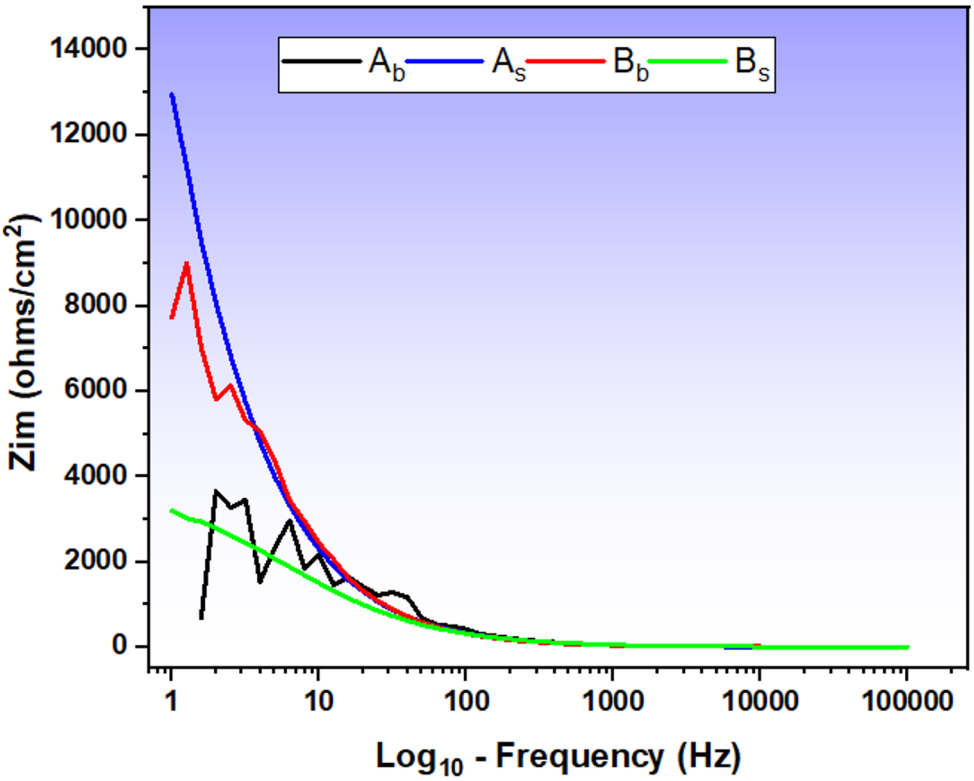

Fig. 3. EIS curves for the built and substrate samples immersed in a typical seawater.

3.1.3 Cyclic potentiodynamic polarization (CPP)

Figure 4 reveals the CPP curves for both of the built regions and substrates, which were achieved by immersing the samples A_b, A_s, B_b and B_s in natural seawater. As stated in the experimental procedures section, the examinations were repeated three times, and only the averaged data for each sample was used to plot the curves shown in Fig. 4. The CPP curve reveals that the curves of the built and substrate samples had some variations in them. The mean values of the various electrochemical parameters acquired from these curves are presented in Table 2.

In evaluating these values, the analysed sample parameters did give some significant variations. Hence, the average value of the corrosion potential (E_{corr}) for the built A_b is -0.679 V and for its substrate A_s is -1.270 V, while the built and substrate samples B_b and B_s are -0.840 V and -1.293 V, respectively. The pitting potential corrosion (E_{pit}) had the following values: A_b, A_s, B_b, and B_s, as 0.471 V, 0.489 V, 0.475 V, and 0.451 V respectively. The variation in these values were attributed to many factors, such as the microstructural differences, varying elemental distribution and compositions, residual stresses, surface roughness, porosity and defects [23, 24]. According to Esmailzadeh et al. (2018) [25] stated that valuable understandings can be achieved by analysing the reverse scan area of the CPP curves. Figure 4 revealed the curves have a significant decrement in the current density at the commencement of the reverse scan, especially when examining samples A_b, B_b, and B_s. This reduction is indicative of the initiation of the repassivation mechanism, in which previously developed pits commence to heal as the potential is decreased. Also, the polarization curves

of these samples displayed positive hysteresis loops, revealing the reverse scan were situated at a higher current density than the forward scan. Thus, this supported the the localized disintegration and partial recovery performance of the alloy surfaces during the corrosion cycle. This behaviour shows that during the reverse potential scan, the complete repassivation of the pits developed was not attained at potentials beyond the pitting potential (Epit). Similarly, this typical experience was achieved by Forcellese et al (2025) [26] and Klapper & Rebak (2017) [27]. Conversely, the A_s, revealed a negative hysteresis loop, which indicated that despite the initiation of pitting at high potentials, the alloy depicts a significant repassivation efficiency by successfully evading pit spread, this observation was similarly reported by Forcellese et al (2025) [26] during their study on localized corrosion in a component fabricated through material extrusion. The obvious decline in the reverse scan current points to the material's ability to recover localized breakdown areas, thus rejecting pinhole development and improving its overall corrosion resistance. This performance indicated that the alloy surface remains passivated even after minor breakdowns, making it more reliable in corrosive environments [28].

The difference between the corrosion potential (E_{corr}) and the pitting potential (E_{pit}), given as $|E_{corr} - E_{pit}|$, offers valuable insight into individual sample's resistance to pitting corrosion. A larger value reveals that a higher shift in potential is needed to promote pitting, which indicates greater resistance to localized attack [29]. Among the samples, A_s showed the greatest resistance to pitting corrosion, with a $|E_{corr} - E_{pit}|$ of about 1.759 V, followed closely by B_s with 1.744 V. The high values observed for the substrate samples (A_s and B_s) indicate that they maintain a stable passive film and are less prone to significant pitting or delamination under typical conditions [27]. In contrast, the built samples A_b and B_b displayed lesser $|E_{corr} - E_{pit}|$ values, measured to be between 1.150 V and 1.315 V respectively. These lower differences reveal that pitting corrosion could potentially develop more easily in these samples, pointing to a decreased passivation ability and higher susceptibility in harsh environments such as chloride-containing solutions. Generally, the substrates samples depicted superior pitting resistance in contrast to their built counterparts, which confirmed that the processing or structural modifications in the substrate materials did attribute immensely to their enhanced corrosion resistance [17].

Table 2. The evaluated corrosion parameter achieved through Tafel extrapolation from polarization curves.

Samples		E_{corr} (V)	E_{pit} (V)	$\|E_{corr} - E_{pit}\|$ (V)	E_{rep} (V)	I_{rep} (A/cm^2)
Sample A	A_b	-0.679	0.471	1.150	-	-
	A_s	-1.27	0.489	1.759	-0.637	0.348
Sample B	B_b	-0.84	0.475	1.315	-	-
	B_s	-1.293	0.451	1.744	-	-

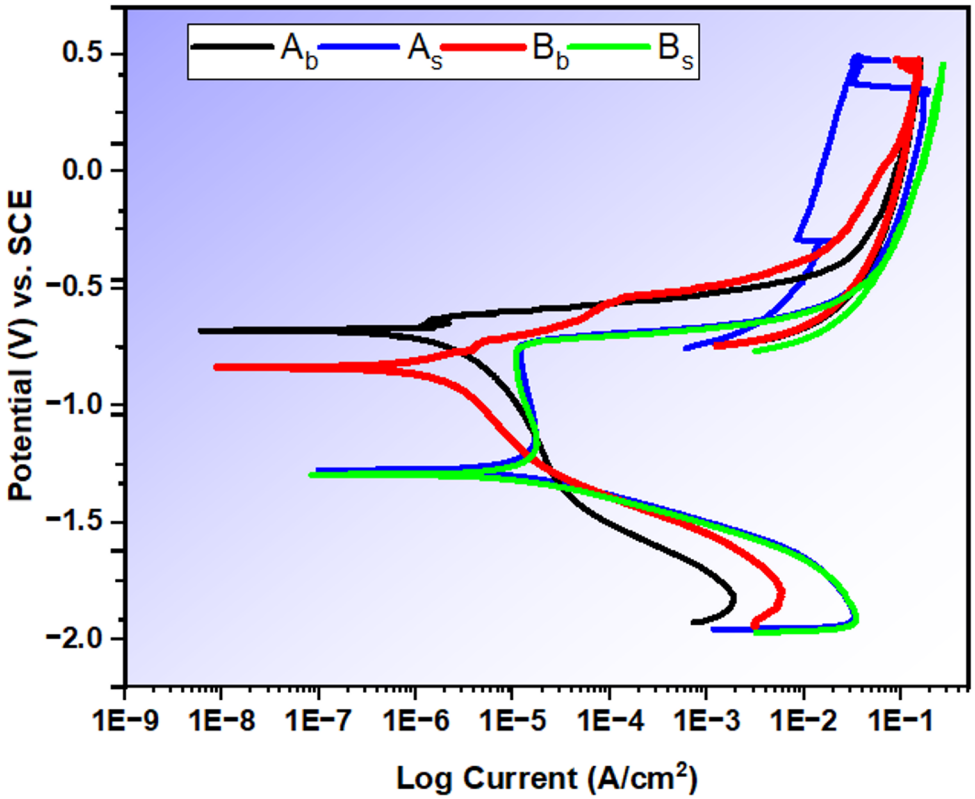

Fig. 4. Cyclic potentiodynamic polarization curves for the built and substrate samples immersed in a typical seawater.

3.2 Microstructural analysis

Qualitative analyses into the specific corrosion behaviors (particularly pitting and others like cracking and delamination) of the samples were conducted by examining their surface microstructural changes before and after electrochemical testing.

Figure 5 presents SEM images of the samples prior to electrochemical testing, revealing observable microstructural variations. The images revealed varying levels of surface porosity, which typically results from entrapped gas diffusion during solidification, which may serve as initiation sites for pitting corrosion [18]. A_s had a uniform grain structure and various low-angle grain boundaries, which are often characterized with lower energy states and improved corrosion resistance [15, 16]. B_s displayed a more merged structure, with an increased high-angle boundaries presence, which was indicative of moderate to lower resistance. The B_b and A_b samples in contrast showed elongated grains and a mark of texture anisotropy achieved from the layer-by-layer manufacturing procedure, along with greater high-angle boundaries, properties usually associated with decreased corrosion resistance and compromised structural integrity [19].

After corrosion exposure, noticeable surface damage was detected, as seen in Fig. 6. Sample A_s remained largely intact, depicting only minor oxide development and minimal localized corrosion (pitting) as reflected in the composition data presented in Table 7. The limited cracking and localized grain boundary corrosion, as well as the preserved microstructural continuity in sample B_s indicated sustained structural integrity. B_b demonstrated some surface oxidation and uniform corrosion characteristics, with some

cracks and pitting detected, indicating a lower corrosion resistance than the substrate sections. Sample A_b was severely degraded with extensive delamination, pitting and unstable oxide film, characteristic of a material more susceptible to corrosion [21].

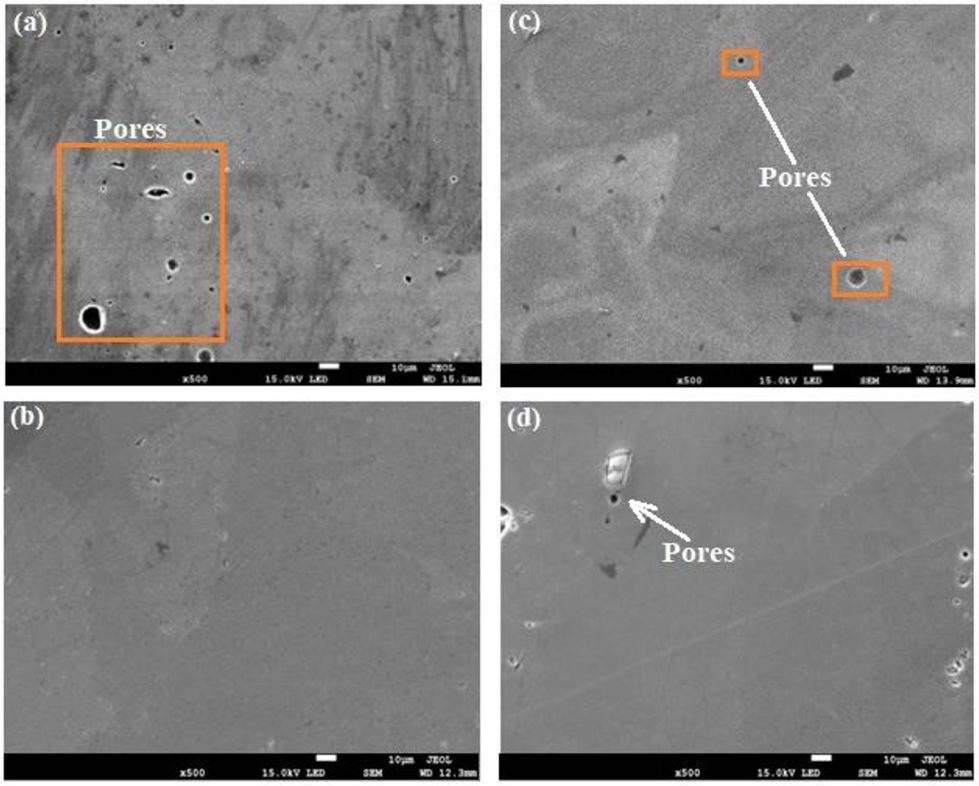

Fig. 5. SEM-SE images of the cross-section samples: (a) A_b, (b) A_s, (c) B_b and (d) B_s before exposure to corrosion.

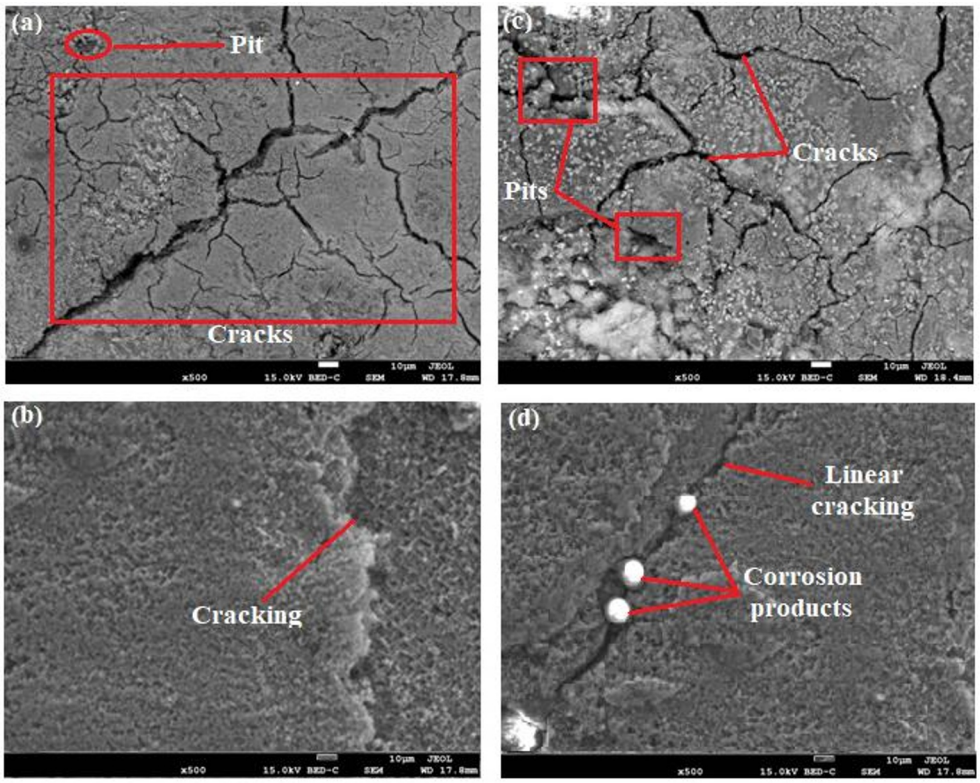

Fig. 6. SEM-SE images of the samples after corrosion: (a) A_b, (b) A_s, (c) B_b and (d) B_s, depicting variances of pitting zones and cracks.

Table 2. Elemental composition (wt%) of each sample after corrosion obtained by EDS analysis

Samples	**Al (wt%)**	**O (wt%)**	**Mg (wt%)**	**Ca (wt%)**	**Si (wt%)**	**Cl (wt%)**	**Na (wt%)**	**S (wt%)**	**Traces of elements, excluded due to conc.** <1 wt%
A_b	17.3	54.6	12.2	3.7	9.4	1.9	—	—	S
A_s	66.8	15.8	—	—	—	—	—	—	S and Mg
B_b	32.3	48.3	2.7	—	12.3	—	3.0	1.2	Ca
B_s	67.5	24.1	1.2	1.5	3.1	—	—	1.3	Fe and Cl

4 Conclusion

In this study, the corrosion performance of HAM Al-alloys was evaluated at the built and substrate sections via OCP, CPP and EIS supported by pre- and post-corrosion surface examinations through SEM-EDS analysis. The outcomes evidently showed that the substrate regions (A_s and B_s) exhibited more stable values, lower corrosion currents, optimal polarization resistance with minimal surface deterioration. This was in direct contrast to the built regions (A_b and B_b), which revealed delamination, pitting, severe cracking, and uneven oxide formation.

Thus, the corrosion resistance, which followed the hierarchy $A_s > B_s > B_b > A_b$, pinpointed to the necessity of essential microstructural properties related to surface stability and grain boundaries. This work highlights that although AM provides flexibility in manufacturing, maintaining microstructural consistency during the process is essential for achieving optimal corrosion resistance in harsh environments. Generally, HAM structures benefit from the complementary properties of the SLM-build and cast substrate regions, which together contribute to enhanced corrosion performance.

The authors gratefully acknowledge the University of Johannesburg, South Africa, for its support. This research was conducted with the assistance of the Centre for Nanoengineering and Advanced Materials, University of Johannesburg.

References

1. J. Jiang, X. Xu, J. Stringer, Rob, Optimization of process planning for reducing material waste in extrusion based additive manufacturing. Comput.-Integr. Manuf. **59**, 317 (2019). https://doi.org/10.1016/j.rcim.2019.05.007
2. N. I. Kolobnev, L. B. Ber, L. B. Khokhlatova, D. K. Ryabov, Structure, properties and application of alloys of the Al–Mg–Si–(Cu) system. Met. Sci. Heat Treat. **53**(9) 440-444 (2012). https://doi.org/10.1007/s11041-012-9412-8
3. T. Peng, K. Kellens, R. Tang, C. Chen, G. Chen, Sustainability of additive manufacturing: An overview on its energy demand and environmental impact. Addit. Manuf. **21**, 694 (2018). https://doi.org/10.1016/j.addma.2018.04.022
4. E.M. Sefene, Y.M. Hailu, A.A. Tsegaw, Metal hybrid additive manufacturing: state-of-the-art. Prog. Addit. Manuf. **7**, 737 (2022).
5. I. H. ZainElabdeen, L. Ismail, O. F. Mohamed, K. A. Khan, and A. Schiffer, Recent advancements in hybrid additive manufacturing of similar and dissimilar metals via laser powder bed fusion. Mater. Sci. Eng. A **909**, 146833 (2024). https://doi.org/10.1016/j.msea.2024.146833
6. E. Eloise, Integration of substrate in aluminium wire and arc additive manufacturing, Ph.D. thesis, Cranfield University (2019).
7. O. E. Hudak et al., Pitting corrosion–Preferred chloride diffusion pathways in physical vapor deposited AlCrN coatings. Corros. Sci. **211**, 110901 (2023). https://doi.org/10.1016/j.corsci.2022.110901
8. P. Can, W. Chuan, W. Zhen-yao, and S. U. N. Cheng, Corrosion and pitting behavior of pure aluminum 1060 exposed to Nansha Islands tropical marine atmosphere. Trans. Nonferrous Met. Soc. China **32**(2), 448–460 (2022). https://doi.org/10.1016/S1003-6326(22)65806-0
9. D.R. Ramya, R.D. Pruthviraj, Potentiodynamic Studies of Aluminium 2024 Alloy in Different Concentration of Hydrochloric Acid Medium at Laboratory Temperature. J. Mater. Sci., **10**, 2321 (2017). https://DOI.org/10.4172/2321-6212.1000199

10. F.V. Adams, S.O. Akinwamide, B. Obadele, P.A. Olubambi, Comparison study on the corrosion behavior of aluminum alloys in different acidic media. Mater. Today: Proc., **38**, 1040 (2021). https://doi.org/10.1016/j.matpr.2020.05.781
11. S.A. Raza, M.R.A. Karim, T. Shehbaz, A.A. Taimoor, R. Ali, M.I. Khan, Effect of pH and concentration on electrochemical corrosion behavior of aluminum Al-7075 T6 alloy in NaCl aqueous environment. J. Electrochem. Sci. Technol., **13**, 213 (2022).
12. L. Kučerová**,** I. Zetková**,** Š. Jeníček**,** K. Burdová, Hybrid parts produced by deposition of 18Ni300 maraging steel via selective laser melting on forged and heat treated advanced high strength steel. *Addit. Manuf.* **32**, 101108 (2020). https://doi.org/10.1016/j.addma.2020.101108
13. S. Shakerin**,** A. Hadadzadeh**,** B.S. Amirkhiz**,** S. Shamsdini**,** J. Li**,** M. Mohammadi, Additive manufacturing of maraging steel-H13 bimetals using laser powder bed fusion technique. *Addit. Manuf.* **29**, 100797 (2019).
14. Y. Uematsu**,** T. Kakiuchi**,** M. Nakajima**,** K. Matsuo, Microstructures and fatigue behavior of additively manufactured maraging steel deposited on conventionally manufactured base plate. *J. Mater. Eng. Perform.* **30**, 4902-4910 (2021). https://doi.org/10.1007/s11665-021-05548-z
15. M. Stefanoni**,** U. Angst**,** B. Elsener, Local electrochemistry of reinforcement steel–distribution of open circuit and pitting potentials on steels with different surface condition. *Corros. Sci.* **98**, 610-618 (2015). https://doi.org/10.1016/j.corsci.2015.06.004.
16. S. Choudhary**,** A. Garg**,** K. Mondal**,** Relation between open circuit potential and polarization resistance with rust and corrosion monitoring of mild steel. *J. Mater. Eng. Perform.* **25**, 2969-2976 (2016). https://doi.org/10.1007/s11665-016-2112-6
17. S. Sahu**,** Pitting Corrosion Behavior of Multi Principal Element Alloys and Understanding Crystallographic Pit Morphologies (2022). http://orcid.org/0000-0003-3052-9442
18. Y. Tan, Sensing Localised Corrosion by Means of Electrochemical Noise Detection and Analysis, *Sens. Actuators B: Chem.* **139**(2), 688-698 (2009). https://doi.org/10.1016/j.snb.2009.03.061
19. F. Andreatta**,** H. Terryn**,** J.H.W. De Wit, Corrosion Behaviour of Different Tempers of AA7075 Aluminium Alloy, *Electrochim. Acta* **49**(17-18), 2851-2862 (2004). https://doi.org/10.1016/j.electacta.2004.01.046
20. V. Encinas-Sánchez**,** M.T. De Miguel**,** M.I. Lasanta**,** G. García-Martín**,** F.J. Pérez, *Sol. Energy Mater. Sol. Cells* **191**, 157-163 (2019). https://doi.org/10.1016/j.solmat.2018.11.007
21. H.H. Hernández**,** A.M.R. Reynoso**,** C. Juan**,** T. González**,** C.O.G. Morán**,** *Electrochem. Impedance Spectrosc.* **1**, 1 (2020)
22. M.C. Li**,** Y.F. Cheng, *Electrochim.* Corrosion of the stressed pipe steel in carbonate–bicarbonate solution studied by scanning localized electrochemical impedance spectroscopy. *Acta* **53**(6), 2831-2836 (2008). https://doi.org/10.1016/j.electacta.2007.10.077
23. C. Ye**,** C. Zhang**,** J. Zhao**,** Y. Dong, Effects of post-processing on the surface finish, porosity, residual stresses, and fatigue performance of additive manufactured metals: a review. *J. Mater. Eng. Perform.* **30**, 6407-6425 (2021). https://doi.org/10.1007/s11665-021-06021-7
24. J. Fu**,** H. Li**,** X. Song**,** M.W. Fu, Multi-scale defects in powder-based additively manufactured metals and alloys. *J. Mater. Sci. Technol.* **122**, 165-199 (2022). https://doi.org/10.1016/j.jmst.2022.02.015

25. S. Esmailzadeh**,** M. Aliofkhazraei**,** H. Sarlak, Interpretation of cyclic potentiodynamic polarization test results for study of corrosion behavior of metals: a review. *Prot. Met. Phys. Chem. Surf.* **54**, 976-989 (2018). https://doi.org/10.1134/S207020511805026X
26. P. Forcellese**,** T. Mancia**,** M. Simoncini**,** T. Bellezze**,** Characterization of Microstructure and Localized Corrosion Resistance of Heat-Treated 17-4 PH Stainless Steel Fabricated by Material Extrusion. *Metals* **15**(2), 137 (2025). https://doi.org/10.3390/met15020137
27. H.S. Klapper**,** R.B. Rebak**,** Assessing the pitting corrosion resistance of oilfield nickel alloys at elevated temperatures by electrochemical methods. *Corrosion* **73**(6), 666-673 (2017). https://doi.org/10.5006/2161
28. C.G. Tiburcio**,** F.H.E. López**,** P.Z. Robledo**,** J.A. Cabral**,** M.C.B. Durtewitz**,** F.A. Calderon, *Int. J. Electrochem. Sci.* **11**(2), 1080-1091 (2016).
29. H.S. Klapper**,** S. Jesse**,** A. Heyn, Electrochemical Methods for Assessing the Pitting Corrosion Resistance of Metallic Materials in Chloride-Containing Environments at Elevated Temperatures (2018). https://doi.org/10.5006/C2018-11438